PAPER

B$_{31}^-$ and B$_{32}^-$: chiral quasi-planar boron clusters†

Qiang Chen,‡[a] Teng-Teng Chen,‡[b] Hai-Ru Li,[a] Xiao-Yun Zhao,[a] Wei-Jia Chen,[b] Hua-Jin Zhai, ![ID] *[a] Si-Dian Li ![ID] *[a] and Lai-Sheng Wang ![ID] *[b]

Chirality plays an important role in nature. Nanoclusters can also exhibit chiral properties. We report herein a joint experimental and theoretical investigation on the geometric and electronic structures of B$_{31}^-$ and B$_{32}^-$ clusters, using photoelectron spectroscopy in combination with first-principles calculations. Two degenerate quasi-planar chiral C_1 enantiomers (**I** and **II**, ^{1}A) with a central hexagonal vacancy are identified as the global minima of B$_{31}^-$. For B$_{32}^-$, two degenerate boat-like quasi-planar chiral C_2 structures (**VI** and **VII**, ^{2}A) with a central hexagonal vacancy are also found as the global minima, with a low-lying chair-like C_i B$_{32}^-$ (**VIII**, ^{2}A$_u$) also present in the experiment as a minor isomer. The chiral conversions in quasi-planar B$_{31}^-$ and B$_{32}^-$ clusters are investigated and relatively low barriers are found due to the high flexibility of these monolayer clusters, which feature multiple delocalized σ and π bonds over buckled molecular surfaces.

1. Introduction

Elemental boron forms diverse bulk allotropes with a variety of three-dimensional (3D) cage-like structural units, such as the B$_{12}$ icosahedron, as building blocks to compensate for its electron deficiency.[1–3] In contrast to bulk boron, systematic combined photoelectron spectroscopy (PES) and quantum chemistry studies in the past two decades have shown that the global-minimum (GM) structures of anionic boron clusters (B$_n^-$) are planar or quasi-planar in an unexpectedly wide range of sizes (n = 3–30, 33–38).[4–28] Chemical bonding analyses reveal that both localized peripheral two-center-two-electron (2c–2e) B–B σ-bonds and delocalized interior multicenter (mc-2e) σ- and π-bonds play important roles in stabilizing these two-dimensional (2D) B$_n^-$ clusters, giving rise to multiple aromaticity and antiaromaticity in boron clusters.[6–8,29] Moreover, based on the similarity of π-bonding patterns between 2D boron clusters and polycyclic aromatic hydrocarbons (PAHs), the concept of all-boron analogues of PAHs has been proposed.[8,11–14,19–22,29]

All 2D B$_n^-$ clusters consist of B$_3$ triangles, with tetragonal, pentagonal, or hexagonal vacancies appearing as defects at certain sizes. There is a tendency for the vacancy sizes to increase from tetragonal, pentagonal, to hexagonal as the cluster size increases. In the smaller size regime, B$_n^-$ (n = 11, 15, 17, 19) clusters[6,12,13] were found to contain one or more tetragonal vacancies, while B$_{20}^-$, B$_{21}^-$, and B$_{23}^-$–B$_{25}^-$ all possessed pentagonal vacancies.[9,14–17] The B$_{36}^{-/0}$ clusters were the first quasi-planar boron clusters that contain a perfect central hexagonal vacancy, providing the first experimental evidence for the viability of extended two-dimensional all-boron sheets named borophenes.[22] Following this work, the B$_{30}^-$ cluster was found to be the first quasi-planar chiral boron cluster with two degenerate enantiomers possessing a relatively low conversion barrier.[18] The smallest quasi-planar B$_n^-$ with a hexagonal vacancy was B$_{26}^-$,[26] while 2D boron clusters with a double hexagonal vacancy (DHV) were observed in B$_{35}^-$, B$_{37}^-$, and B$_{38}^-$,[20,27] unveiling more flexible embryos for borophenes with adjacent hexagonal vacancies and different vacancy densities.[20] Borophenes were recently successfully synthesized on an Ag(111) substrate.[30,31]

More intriguingly, the first experimental observation and characterization of all-boron fullerenes, B$_{40}^{-/0}$, dubbed borospherenes,[32] were reported in 2014. Although the B$_{40}^-$ borospherene is slightly higher in energy than a 2D structure with a DHV, neutral B$_{40}$ borospherene is overwhelmingly the GM on the potential energy surface. The first axially chiral borospherenes (C_3/C_2 B$_{39}^-$) were observed shortly after as well-defined GM structures.[33] Seashell-like C_2 B$_{28}^-$ and C_s B$_{29}^-$ borospherenes[24,25] were also identified experimentally as minor isomers, which compete with a close-packed 2D B$_{28}^-$ and a stingray-shaped 2D B$_{29}^-$ with a pentagonal vacancy, respectively. Clearly, B$_n^-$ boron clusters in the size region of n = 26–38 exhibit a complicated structural landscape, featuring

^{a}*Nanocluster Laboratory, Institute of Molecular Science, Shanxi University, Taiyuan 030006, China. E-mail: hj.zhai@sxu.edu.cn, lisidian@sxu.edu.cn*
^{b}*Department of Chemistry, Brown University, Providence, Rhode Island 02912, USA. E-mail: lai-sheng_wang@brown.edu*
†Electronic supplementary information (ESI) available. See DOI: 10.1039/c9nr01524h
‡These authors contributed equally to this work.

competition between 2D structures with a single hexagonal vacancy, 2D structures with a DHV, and 3D seashell-like low-lying isomers at $n = 28$ and 29. This situation presents a huge challenge in the characterization of B_{31}^- and B_{32}^- clusters, the last two anionic boron clusters that remain to be experimentally characterized to date in the size range $n \leq 40$, owing to their complex PES spectra and complicated potential energy surfaces. For them, 2D structures with a single hexagonal vacancy or a DHV, as well as 3D structures, all seem possible.

To fill in the gap and fully characterize all the B_n^- ($n \leq 40$) clusters, we present herein a joint investigation into the geometric and electronic structures of B_{31}^- and B_{32}^- using PES and first-principles calculations. Two degenerate quasi-planar chiral C_1 enantiomers (**I** and **II**, ^1A) with a central hexagonal vacancy are identified as the GM structures of B_{31}^-, with a C_1 transition state located on the conversion pathway. Two degenerate boat-like chiral C_2 B_{32}^- (**VI** and **VII**, ^2A) with a central hexagonal vacancy were also found as the GM structures of B_{32}^-, along with a 2D chair-like local minimum C_i B_{32}^- (**VIII**, ^2A_u) as a minor isomer coexisting experimentally. Two degenerate C_1 transition states as a pair of enantiomers are located between the observed C_2 GM and the C_i isomer. The chiral conversions in quasi-planar B_{31}^- and B_{32}^- occur via the buckling of flexible molecular planes, making these species unique in 2D boron clusters.

2. Methods

2.1 Photoelectron spectroscopy

The experiments were carried out using a magnetic-bottle PES apparatus equipped with a laser vaporization supersonic source. Details of the experimental setup have been described elsewhere.[19,34] Briefly, boron anion clusters (B_n^-) were generated by the laser vaporization of a hot-pressed ^{11}B-enriched boron disk target using He carrier gas seeded with 5% Ar. The cooling of the clusters was controlled by the time delay between the pulsed valve and the vaporization laser, as well as by the residence time of clusters in the nozzle.[19] Negatively charged boron clusters were extracted perpendicularly from the molecular beam and analyzed using a time-of-flight mass spectrometer. The B_{31}^- and B_{32}^- clusters were mass selected and decelerated before photodetachment by the 193 nm (6.424 eV) radiation from an ArF excimer laser. Photoelectrons were collected at nearly 100% efficiency by the magnetic bottle and analyzed in a 3.5 m long electron flight tube. The PES spectrum was calibrated using the known spectrum of Bi^- and the resolution of the PES apparatus was $\Delta E_k/E_k \approx 2.5\%$, that is, ~25 meV for 1 eV kinetic energy electrons.

2.2 Theoretical methods

The GM searches were performed on B_{31}^- and B_{32}^- clusters using the TGMin code[35,36] at the DFT level, in conjunction with manual structural constructions based on the known planar, cage-like, and tubular boron cluster motifs. By running TGMin searches from independent initial structures, we

obtained more than 5400 and 4000 structures for B_{31}^- and B_{32}^-, respectively. Low-lying isomers were then fully optimized at the PBE0/6-311+G(d) level.[37,38] Vibrational frequencies were calculated to ensure that the reported isomeric structures are true minima on the potential energy surfaces. Single-point energies of the five lowest-lying isomers were further refined at PBE0 geometries using the coupled cluster CCSD(T) method[39–41] implemented in MOLPRO 2012.[42] The vertical detachment energies (VDEs) for excited states were calculated using time-dependent DFT (TD-DFT)[43] with the PBE0 functional. Bonding analyses were performed using the adaptive natural density partitioning (AdNDP) approach at the PBE0/6-31G(d)//PBE0/6-311+G(d) level.[44] All optimizations were performed using the Gaussian 09 package.[45]

3. Experimental results

The PES spectra of B_{31}^- and B_{32}^- at 193 nm are shown in Fig. 1a and 2a, respectively, compared to the simulated spectra of their respective GM structures. The observed spectral bands are labelled with the letters (X, A, B, ...). The lowest binding energy band (X) corresponds to the transition from the ground state of B_n^- to that of the corresponding neutral, whereas the higher binding energy bands (A, B, C, ...) correspond to detachment transitions to excited states of the neutral species. All measured VDEs and adiabatic detachment energies (ADEs) are listed in Tables S1 and S2 in the ESI,† where they are compared with the calculated VDEs and ADEs at the PBE0 level.
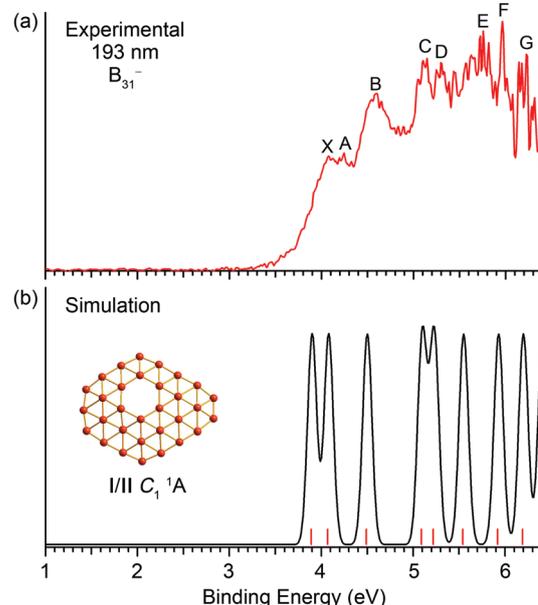

Fig. 1 Photoelectron spectrum of B_{31}^- at 193 nm (a) compared with the simulated spectra of the lowest-lying isomers of B_{31}^- (C_1, **I** and **II**) (b) at the TD-PBE0/6-311+G(d) level. The simulated spectra were obtained by fitting the calculated VDEs (vertical red bars) with unit-area Gaussian functions of 0.05 eV half-width.

Fig. 2 Photoelectron spectrum of B_{32}^- at 193 nm (a) compared with the simulated spectra of the lowest-lying isomers of B_{32}^- (C_2, **VI** and **VII**) (b) and a low-lying isomer B_{32}^- (C_i, **VIII**) (c) at the TD-PBE0/6-311+G(d) level. The simulated spectra were obtained by fitting the calculated VDEs (vertical red bars) with unit-area Gaussian functions of 0.05 eV half-width.
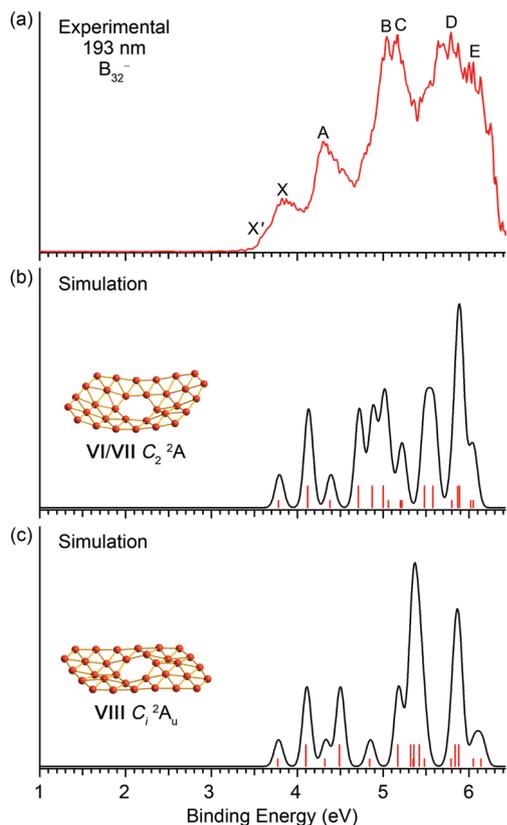
3.1 Photoelectron spectrum of B_{31}^-

As shown in Fig. 1a, a series of PES spectral bands are resolved for B_{31}^-. Band X yields the first VDE at 4.07 eV. The first ADE was evaluated to be 3.74 eV from its onset, which represents the electron affinity (EA) of neutral B_{31}. Peak A at 4.24 eV partially overlaps with peak X. Band B, centered at 4.60 eV, is sharper and well separated from bands X and A. Following an energy gap of about 0.5 eV, two closely spaced bands C (5.11 eV) and D (5.30 eV) are observed. At the higher energy part beyond 5.5 eV, the signal-to-noise ratio is poor: a sharp band F is observed at 6.00 eV, while band E at around 5.7 eV and band G at ~6.2 eV are tentatively assigned.

3.2 Photoelectron spectrum of B_{32}^-

The 193 nm PES spectrum of B_{32}^- consists of six relatively broad bands, labelled as X and A–E (Fig. 2a). The lowest binding energy band X gives the first VDE at 3.82 eV and an estimated first ADE at 3.65 eV from its onset. There is a weak shoulder X' (VDE: 3.57 eV) at the low binding energy side, which may come from a minor isomer of B_{32}^-. Band A (VDE: 4.30 eV) is well separated from band X. Following a large gap, two intense and closely spaced bands B (5.04 eV) and C (5.17 eV) are observed. Above 5.5 eV, the spectrum is congested, and

bands D (~5.8 eV) and E (~6.1 eV) are tentatively labelled for the sake of discussion.

4. Computational results

We searched for the GM and low-lying isomers of B_{31}^- and B_{32}^- by employing the TGMin code. The resulting isomers were then re-optimized at the PBE0/6-311+G(d) level. The lowest 20 structures of B_{31}^- and B_{32}^- at PBE0 are shown in Fig. S1 and S2,† respectively. All the structures were determined to be true minimum without imaginary frequencies. Low-lying isomers of B_{31}^- and B_{32}^- within 0.5 eV at PBE0 were further refined at the single-point CCSD(T) level. The five lowest-lying structures of B_{31}^- and B_{32}^- are shown in Fig. 3(a) and (b) and the Cartesian coordinates are given in Table S3.†

4.1 Global minima and low-lying isomers of B_{31}^-

We found that the GM structures of B_{31}^- are two degenerate quasi-planar ones, **I** and **II** (C_1, ^{1}A; Fig. 3a), which are a pair of chiral enantiomers with a central hexagonal vacancy. Both structures are composed of seventeen peripheral and fourteen interior atoms with an out-of-plane buckling of 1.52 Å. They can be obtained by removing two edge atoms of the previously observed GM for B_{33}^-.[28] The third isomer **III** (C_2, ^{1}A) is a 3D seashell-like cage structure similar to the B_{28}^- and B_{29}^- borospherenes,[24,25] which lie slightly higher (by 0.08 eV) than the GM structures at the CCSD(T) level. The fourth isomer **IV** (C_s, ^{1}A') with a DHV is found to be 0.12 eV higher in energy at CCSD(T), and it is related to the experimentally identified 2D B_{35}^- cluster[20] by removing a row of four edge atoms at the bottom. The 2D isomer **V** (C_1 ^{1}A) is calculated to be 0.17 eV above the GM at CCSD(T). Among the lowest 20 isomers of B_{31}^- shown in Fig. S1,† 12 are quasi-planar and 8 are seashell-like, indicating that there is a competition between the 2D structures and 3D cages at this size.

4.2 Global minimum and low-lying isomers of B_{32}^-

The GM structures of B_{32}^- are also a pair of quasi-planar degenerate chiral enantiomers with a boat-like shape and a
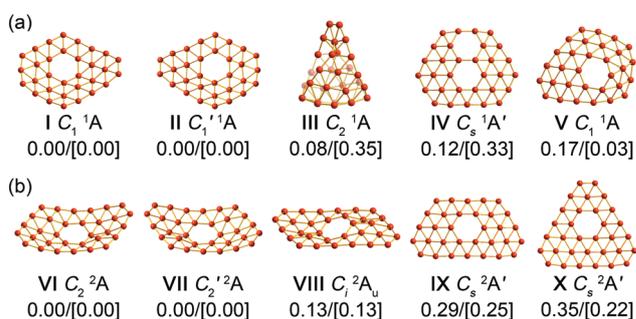

Fig. 3 Top five lowest-lying isomers of B_{31}^- (a) and B_{32}^- (b). Relative energies are given in eV at CCSD(T)//PBE0 and PBE0/6-311+G(d) (in square brackets) levels. Single-point calculations for top five lowest-lying isomers of B_{31}^- and B_{32}^- were carried out using CCSD(T)/6-311G(d) and UCCSD(T)/6-31G(d), respectively.

central hexagonal vacancy, **VI** and **VII** (C_2, ^{2}A) in Fig. 3b. A chair-like isomer **VIII** (C_i, ^{2}A$_u$), which is 0.13 eV higher in energy at CCSD(T), can be viewed as a conformational isomer of boat-like **VI** and **VII**, similar to the chair- and boat-like cyclohexanes. These three isomers are all related to the second isomer of the B_{27}^- cluster[23] by adding a B_5 double chain along one of the tetratomic edges. The structural differences between boat and chair conformers lie in the buckling within the molecular plane. Both boat-like **VI** and **VII** enantiomers possess an out-of-plane buckling of 1.55 Å. Quasi-planar **IX** (C_s, ^{2}A′) and **X** (C_s, ^{2}A′) lie 0.29 eV and 0.35 eV above the GM structures of B_{32}^- at CCSD(T), respectively. These higher lying isomers also contain a central hexagonal vacancy, but with different structural arrangements compared to boat- and chair-like B_{32}^-. The top five isomers all consist of eighteen peripheral atoms and fourteen interior atoms. A tubular isomer (D_8, ^{2}A$_1$; Fig. S2†) is 0.36 eV higher in energy at the PBE0 level. Different from the B_{31}^- cluster, the potential energy surface of B_{32}^- is entirely dominated by 2D structures, as reflected by the fact that the top 20 lowest-lying isomers of B_{32}^- are all quasi-planar, except the tubular one.

5. Discussion

5.1 Comparison between experiment and theory

The PES spectrum can be viewed as an electronic fingerprint for the underlying anionic cluster. In order to confirm the GM structures of B_{31}^- and B_{32}^-, the VDEs of the predicted low-lying isomers of B_{31}^- (**I–V**) and B_{32}^- (**VI–VIII**) were calculated using TD-DFT with the PBE0 functional and they are compared with the experimental VDEs in Tables S1 and S2,† respectively. The computed VDEs are used to produce the simulated spectra by fitting each VDE with a unit-area Gaussian, which are compared with the experimental spectra in Fig. 1, 2 and S3.†

5.1.1 B_{31}^-. As shown in Table S1,† isomer **I** of B_{31}^- and its chiral enantiomer **II** have the same electronic structure, giving a set of entirely identical VDEs. The first and second VDEs of **I/II**, resulting from the removal of an electron from HOMO (47a) and HOMO−1 (46a), are calculated to be 3.89 eV and 4.07 eV, respectively. These two VDEs are close to each other, agreeing with the observed adjacent bands X (4.07 eV) and A (4.24 eV), which are separated by 0.17 eV. The calculated ADE of **I/II** is 3.76 eV, in excellent agreement with the experimental ADE of 3.74 eV. Electron detachment from HOMO−2 (45a) yields a VDE of 4.49 eV, in good agreement with the well-separated band B (4.60 eV). The fourth and fifth detachment channels produce two VDEs of 5.09 and 5.22 eV which are in good agreement with the closely spaced bands C (5.11 eV) and D (5.30 eV). The next three detachment channels are predicted to be between 5.54 and 6.19 eV, which should be assigned to bands E (~5.7 eV), F (6.00 eV), and G (~6.2 eV). Overall, the observed PES patterns of B_{31}^-, in particular, the closely spaced bands X/A and the well-separated band B, can be well reproduced by the simulated spectrum of chiral enantiomers **I** and **II**. The

first two VDEs of isomers **III**, **IV**, and **V** are calculated to be 4.07/4.37, 3.88/4.62, and 3.88/4.47 eV (Table S1†), none of which is consistent with the closely spaced bands X and A. As shown in Fig. S3,† the overall simulated spectral patterns of these low-lying isomers do not agree well with the experiment. Hence, we conclude that the degenerate chiral enantiomers **I** and **II** are the true GM structures of B_{31}^-.

5.1.2 B_{32}^-. Since all low-lying isomers of B_{32}^- are doublet states with an unpaired electron (Fig. 3b and S2†), both singlet and triplet final states are accessible upon one-electron detachment. The first VDE of electron detachment from the singly occupied HOMO (25a) of the predicted GM structures of B_{32}^- is calculated to be 3.78 eV, which is in good agreement with the experimental VDE for band X (3.82 eV). The calculated ADE of 3.70 eV is also in excellent agreement with the measured ADE (3.65 eV). The next two detachment channels come from removal of an electron from HOMO−1 (24a), producing both triplet and singlet final states. The computed VDEs of 4.12 and 4.38 eV for these two channels, respectively, are in good agreement with the broad band A at 4.30 eV. In the regime of 4.71 to 5.22 eV, there are six detachment channels, which are responsible for the intense and overlapping bands B (5.04 eV) and C (5.17 eV). There are also numerous detachment channels at the higher energy side, consistent with the broad bands E and F (Fig. 2b and Table S2†).

The chair-like C_i **VIII** lies only 0.13 eV higher in energy than the boat-like **VI/VII**. Its calculated first VDE of 3.77 eV (Table S2†) appears to be slightly lower than that of **VI/VII** (3.78 eV). In the experimental spectrum, there is a weak shoulder peak X′ at 3.57 eV. Since there exist no other low-lying isomers between **VII** and **VIII**, isomer **VIII** is the only possible species contributing to peak X′ (Fig. 2c). Isomers **IX** and **X** can be safely ruled out from the experiment because of their relatively high energies. Hence, we conclude that the degenerate boat-like chiral pair C_2 **VI/VII** are the main isomers in the cluster beam of B_{32}^-, while the slightly higher lying chair-like **VIII** isomer is present as a minor species.

5.2 Chemical bonding

To understand the stability of the GM structures of B_{31}^- (**I/II**; C_1, ^{1}A) and B_{32}^- (**VI/VII**; C_2, ^{2}A), we analyze their chemical bonding using AdNDP.[44] The AdNDP analyses were done on the closed-shell systems, C_1 B_{31}^-, C_2 B_{32}, and C_2 B_{32}^{2-}, as shown in Fig. 4, 5, and S4,† respectively.

As shown in Fig. 4a, B_{31}^- possesses 17 2c–2e σ bonds on the peripheral B_{17} ring, 6 3c–2e σ bonds around the inner B_6 hexagon, and 14 4c–2e σ bonds between the interior and peripheral rings. In addition, our AdNDP analyses of B_{31}^- uncovered ten multi-center π bonds, which include 2 4c–2e π bonds, 4 5c–2e π bonds, and 4 6c–2e π bonds. The π bonding pattern of B_{31}^- exhibits a one-to-one correspondence to the ten π bonds of the PAH $C_{19}H_{11}^-$ (Fig. 4b). In fact, this π-bonding pattern is identical to that of B_{33}^-,[28] although B_{31}^- possesses three fewer σ bonds. Therefore, B_{31}^- is the second all-boron analog of $C_{19}H_{11}^-$, further reinforcing the analogy between 2D boron clusters and PAHs.[6–8,11–14,19–22,29]
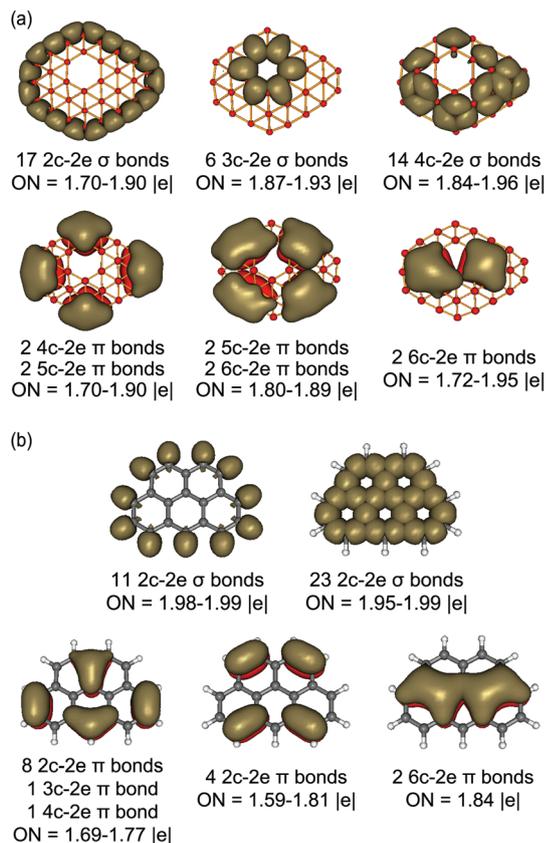
(a)

17 2c-2e σ bonds
ON = 1.70-1.90 |e|

6 3c-2e σ bonds
ON = 1.87-1.93 |e|

14 4c-2e σ bonds
ON = 1.84-1.96 |e|

2 4c-2e π bonds
2 5c-2e π bonds
ON = 1.70-1.90 |e|

2 5c-2e π bonds
2 6c-2e π bonds
ON = 1.80-1.89 |e|

2 6c-2e π bonds
ON = 1.72-1.95 |e|

(b)

11 2c-2e σ bonds
ON = 1.98-1.99 |e|

23 2c-2e σ bonds
ON = 1.95-1.99 |e|

8 2c-2e π bonds
1 3c-2e π bond
1 4c-2e π bond
ON = 1.69-1.77 |e|

4 2c-2e π bonds
ON = 1.59-1.81 |e|

2 6c-2e π bonds
ON = 1.84 |e|

Fig. 4 Comparison of the AdNDP patterns of GM B_{31}^- (a) and PAH $C_{19}H_{11}^-$ (b). ON represents the occupation number.

(a)

18 2c-2e σ bonds
ON = 1.76-1.92 |e|

6 3c-2e σ bonds
ON = 1.87-1.95 |e|

14 4c-2e σ bonds
ON = 1.84-1.95 |e|

2 4c-2e π bonds
6 5c-2e π bonds
ON = 1.63-1.88 |e|

2 6c-2e π bonds
ON = 1.89 |e|

(b)

12 2c-2e σ bonds
ON = 1.98 |e|

24 2c-2e σ bonds
ON = 1.96-1.99 |e|

8 2c-2e π bonds
ON = 1.69-1.73 |e|

2 6c-2e π bonds
ON = 1.83 |e|

Fig. 5 Comparison of the AdNDP patterns for closed-shell C_2 B_{32} (a) and PAH $C_{20}H_{12}$ (b). ON represents the occupation number.

As shown in Fig. 5a, there are also three types of σ bonds in C_2 B_{32}, including 18 peripheral 2c–2e bonds, 6 3c–2e bonds around the hexagonal vacancy, and 14 4c–2e bonds in the molecular framework. The remaining 20 electrons form 10 multi-centre π bonds (2 4c–2e π bonds, 6 5c–2e π bonds, and 2 6c–2e π bonds). The π bonding pattern is analogous to that of PAH perylene ($C_{20}H_{12}$), as shown Fig. 5b. Hence, the B_{32} cluster presents another all-boron analogue of PAHs. With two extra electrons, the closed-shell C_2 B_{32}^{2-} dianion possesses one more 8c–2e π bond than neutral C_2 B_{32} (Fig. S4†). All other σ and π bonds in C_2 B_{32}^{2-} are the same as in neutral C_2 B_{32}.

5.3 Chiral conversions *via* buckling in both B_{31}^- and B_{32}^-

The GM structures of both B_{31}^- and B_{32}^- are chiral due to their quasiplanarity. To better understand the chirality and stability of the enantiomers of B_{31}^- (C_1 **I** and C_1' **II**) and B_{32}^- (C_2 **VI** and C_2' **VII**), we perform extensive searches to locate possible transition states between the enantiomer pairs using the QST2 or QST3 method at the PBE0/6-311+G(d) level. The obtained reaction paths were verified by the intrinsic reaction coordination (IRC)[46] calculations at the same level of theory (Fig. S5 and S6†). As shown in Fig. 6, an almost planar transition state C_1 B_{31}^- (**TS1**) with the imaginary vibrational frequency of 79i cm^{-1} and a small out-of-plane buckling of 0.84 Å is located on the pathway between the two enantiomers of C_1
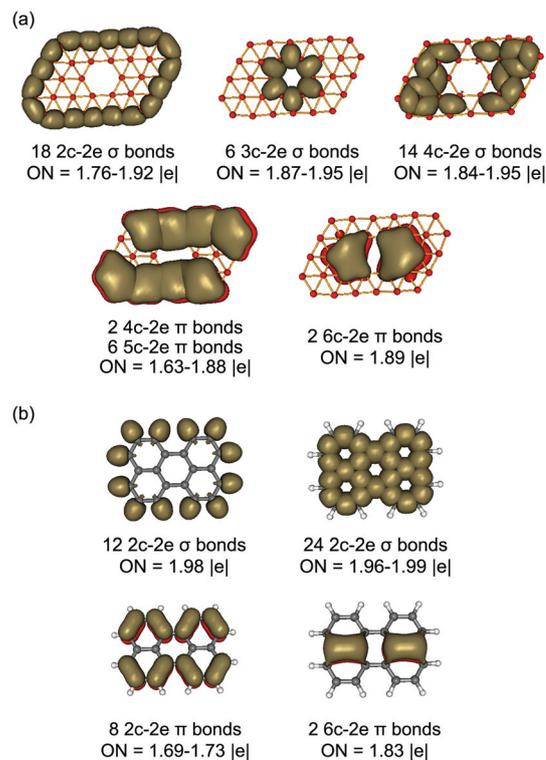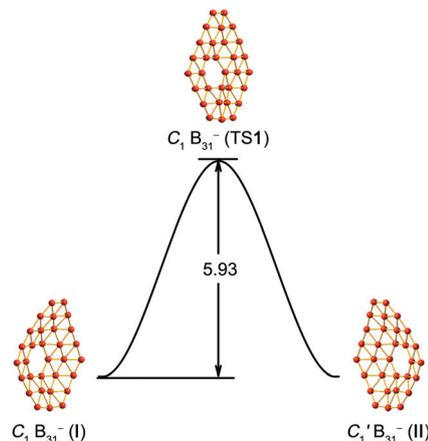

Fig. 6 Chiral conversion between two degenerate enantiomers of B_{31}^- (C_1 **I** and C_1' **II**) *via* buckling through the transition state C_1 B_{31}^- (**TS1**). The relative energy is given in kcal mol^{-1} at the CCSD(T)/6-311G(d)// PBE0/6-311+G(d) level.

B_{31}^- (**I**) and C_1' B_{31}^- (**II**). The chiral conversion energy barrier (ΔE_a) is found to be 5.93 kcal mol^{-1} at CCSD(T), which is similar to the barrier (6.2 kcal mol^{-1}) reported previously for the chiral B_{30}^- cluster.[18] Such an energy barrier well preserves the two enantiomers of B_{31}^- under our experimental conditions at sub-room temperatures.

As shown in Fig. 7, the chiral conversion of B_{32}^- goes through an intermediate non-chiral local minimum (C_i B_{32}^-,
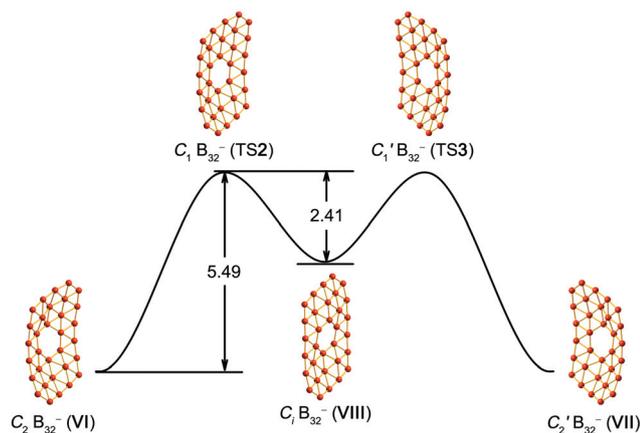
Fig. 7 Chiral conversion between two degenerate enantiomers of B_{32}^- (C_2 **VI** and C'_2 **VII**) through the chair-like intermediate local minimum C_i B_{32}^- (**VIII**) and two transition states C_1 B_{32}^- (**TS2**) and C'_1 B_{32}^- (**TS3**). The relative energy is given in kcal mol^{-1} at the UCCSD(T)/6-31G(d)//PBE0/6-311+G(d) level.

VIII). Two degenerate chiral transition states C_1 B_{32}^- (**TS2**) and C'_1 B_{32}^- (**TS3**) with an imaginary frequency of $53i$ cm^{-1} are located on the pathways between C_2 B_{32}^- (**VI**)–C_i B_{32}^- (**VIII**) and C_i B_{32}^- (**VIII**)–C'_2 B_{32}^- (**VII**), with the forward conversion barriers of ΔE_a = 5.49 and 2.41 kcal mol^{-1}, respectively (Fig. 7). It should be pointed out that there is evidence that the C_i B_{32}^- (**VIII**) isomer is present experimentally (Fig. 2), suggesting that the 2.41 kcal mol^{-1} conversion barrier is sufficient to protect the local minimum under our experimental conditions.

The chirality of B_{31}^- and B_{32}^- is entirely due to the non-planarity of these clusters. Hence, the conversion between enantiomers only involves buckling within the molecular plane, while the positions of the central hexagon and the atomic connectivity remain unchanged along the pathways. The relatively low energy barriers are unique in boron clusters due to delocalized σ and π bonding on the buckled molecular surfaces of B_{31}^- and B_{32}^-. It is interesting to speculate whether chirality in nanoclusters can be extended in two dimensions to form chiral borophenes with distinct optical activities.

6. Conclusions

We report a joint photoelectron spectroscopy and first-principles theoretical investigation on the geometric and electronic structures of B_{31}^- and B_{32}^-, completing the experimental characterization studies of B_n^- clusters in the size range of 3–40 atoms. Two degenerate quasi-planar chiral C_1 enantiomers are confirmed to be the global minima of B_{31}^-, and two degenerate boat-like chiral C_2 B_{32}^- (**VI** and **VII**, ^{2}A) and one chair-like C_i B_{32}^- (**VIII**, ^{2}A$_u$) low-lying isomers are found to coexist experimentally. The unique chiral conversions *via* buckling within the molecular planes of B_{31}^- and B_{32}^- are also investigated and relatively low chiral conversion barriers are revealed. The chair-like low-lying isomer of B_{32}^- is found to be a local minimum along the conversion path of its chiral global minima.

Conflicts of interest

There are no conflicts to declare.

Acknowledgements

Notes and references

1 N. Vast, S. Baroni, G. Zerah, J. M. Besson, A. Polian, M. Grimsditch and J. C. Chervin, *Phys. Rev. Lett.*, 1997, **78**, 693–696.
2 B. Albert and H. Hillebrecht, *Angew. Chem., Int. Ed.*, 2009, **48**, 8640–8668.
3 M. Fujimori, T. Nakata, T. Nakayama, E. Nishibori, K. Kimura, M. Takata and M. Sakata, *Phys. Rev. Lett.*, 1999, **82**, 4452–4455.
4 H.-J. Zhai, L.-S. Wang, A. N. Alexandrova and A. I. Boldyrev, *J. Chem. Phys.*, 2002, **117**, 7917–7924.
5 W.-L. Li, X. Chen, T. Jian, T.-T. Chen, J. Li and L.-S. Wang, *Nat. Rev. Chem.*, 2017, **1**, 0071.
6 H.-J. Zhai, B. Kiran, J. Li and L.-S. Wang, *Nat. Mater.*, 2003, **2**, 827–833.
7 H.-J. Zhai, A. N. Alexandrova, K. A. Birch, A. I. Boldyrev and L.-S. Wang, *Angew. Chem., Int. Ed.*, 2003, **42**, 6004–6008.
8 A. N. Alexandrova, A. I. Boldyrev, H.-J. Zhai and L.-S. Wang, *Coord. Chem. Rev.*, 2006, **250**, 2811–2866.
9 B. Kiran, S. Bulusu, H.-J. Zhai, S. Yoo, X. C. Zeng and L.-S. Wang, *Proc. Natl. Acad. Sci. U. S. A.*, 2005, **102**, 961–964.
10 L.-L. Pan, J. Li and L.-S. Wang, *J. Chem. Phys.*, 2008, **129**, 024302.
11 A. P. Sergeeva, D. Y. Zubarev, H.-J. Zhai, A. I. Boldyrev and L.-S. Wang, *J. Am. Chem. Soc.*, 2008, **130**, 7244–7246.
12 W. Huang, A. P. Sergeeva, H.-J. Zhai, B. B. Averkiev, L.-S. Wang and A. I. Boldyrev, *Nat. Chem.*, 2010, **2**, 202–206.
13 A. P. Sergeeva, B. B. Averkiev, H.-J. Zhai, A. I. Boldyrev and L.-S. Wang, *J. Chem. Phys.*, 2011, **134**, 224304.
14 A. P. Sergeeva, Z. A. Piazza, C. Romanescu, W.-L. Li, A. I. Boldyrev and L.-S. Wang, *J. Am. Chem. Soc.*, 2012, **134**, 18065–18073.
15 Z. A. Piazza, W.-L. Li, C. Romanescu, A. P. Sergeeva, L.-S. Wang and A. I. Boldyrev, *J. Chem. Phys.*, 2012, **136**, 104310.
16 I. A. Popov, Z. A. Piazza, W.-L. Li, L.-S. Wang and A. I. Boldyrev, *J. Chem. Phys.*, 2013, **139**, 144307.

17 Z. A. Piazza, I. A. Popov, W.-L. Li, R. Pal, X. C. Zeng, A. I. Boldyrev and L.-S. Wang, *J. Chem. Phys.*, 2014, **141**, 034303.

18 W.-L. Li, Y.-F. Zhao, H.-S. Hu, J. Li and L.-S. Wang, *Angew. Chem., Int. Ed.*, 2014, **53**, 5540–5545.

19 L.-S. Wang, *Int. Rev. Phys. Chem.*, 2016, **35**, 69–142.

20 W.-L. Li, Q. Chen, W.-J. Tian, H. Bai, Y.-F. Zhao, H.-S. Hu, J. Li, H.-J. Zhai, S.-D. Li and L.-S. Wang, *J. Am. Chem. Soc.*, 2014, **136**, 12257–12260.

21 A. P. Sergeeva, I. A. Popov, Z. A. Piazza, W.-L. Li, C. Romanescu, L.-S. Wang and A. I. Boldyrev, *Acc. Chem. Res.*, 2014, **47**, 1349–1358.

22 Z. A. Piazza, H.-S. Hu, W.-L. Li, Y.-F. Zhao, J. Li and L.-S. Wang, *Nat. Commun.*, 2014, **5**, 3113.

23 W.-L. Li, R. Pal, Z. A. Piazza, X. C. Zeng and L.-S. Wang, *J. Chem. Phys.*, 2015, **142**, 204305.

24 H.-R. Li, T. Jian, W.-L. Li, C.-Q. Miao, Y.-J. Wang, Q. Chen, X.-M. Luo, K. Wang, H.-J. Zhai, S.-D. Li and L.-S. Wang, *Phys. Chem. Chem. Phys.*, 2016, **18**, 29147–29155.

25 Y.-J. Wang, Y.-F. Zhao, W.-L. Li, T. Jian, Q. Chen, X.-R. You, T. Ou, X.-Y. Zhao, H.-J. Zhai, S.-D. Li, J. Li and L.-S. Wang, *J. Chem. Phys.*, 2016, **144**, 064307.

26 X.-M. Luo, T. Jian, L.-J. Cheng, W.-L. Li, Q. Chen, R. Li, H.-J. Zhai, S.-D. Li, A. I. Boldyrev, J. Li and L.-S. Wang, *Chem. Phys. Lett.*, 2017, **683**, 336–341.

27 Q. Chen, W.-J. Tian, L.-Y. Feng, H.-G. Lu, Y.-W. Mu, H.-J. Zhai, S.-D. Li and L.-S. Wang, *Nanoscale*, 2017, **9**, 4550–4557.

28 Q. Chen, W.-L. Li, X.-Y. Zhao, H.-R. Li, L.-Y. Feng, H.-J. Zhai, S.-D. Li and L.-S. Wang, *Eur. J. Inorg. Chem.*, 2017, **2017**, 4546–4551.

29 A. I. Boldyrev and L.-S. Wang, *Phys. Chem. Chem. Phys.*, 2016, **18**, 11589–11605.

30 A. J. Mannix, X. F. Zhou, B. Kiraly, J. D. Wood, D. Alducin, B. D. Myers, X. Liu, B. L. Fisher, U. Santiago, J. R. Guest, M. J. Yacaman, A. Ponce, A. R. Oganov, M. C. Hersam and N. P. Guisinger, *Science*, 2015, **350**, 1513–1516.

31 B. Feng, J. Zhang, Q. Zhong, W. Li, S. Li, H. Li, P. Cheng, S. Meng, L. Chen and K. Wu, *Nat. Chem.*, 2016, **8**, 563–568.

32 H.-J. Zhai, Y.-F. Zhao, W.-L. Li, Q. Chen, H. Bai, H.-S. Hu, Z.-A. Piazza, W.-J. Tian, H.-G. Lu, Y.-B. Wu, Y.-W. Mu, G.-F. Wei, Z.-P. Liu, J. Li, S.-D. Li and L.-S. Wang, *Nat. Chem.*, 2014, **6**, 727–731.

33 Q. Chen, W.-L. Li, Y.-F. Zhao, S.-Y. Zhang, H.-S. Hu, H. Bai, H.-R. Li, W.-J. Tian, H.-G. Lu, H.-J. Zhai, S.-D. Li, J. Li and L.-S. Wang, *ACS Nano*, 2015, **9**, 754–760.

34 L.-S. Wang, H.-S. Cheng and J. Fan, *J. Chem. Phys.*, 1995, **102**, 9480–9493.

35 Y. Zhao, X. Chen and J. Li, *Nano Res.*, 2017, **10**, 3407–3420.

36 X. Chen, Y.-F. Zhao, L.-S. Wang and J. Li, *Comput. Theor. Chem.*, 2017, **1107**, 57–65.

37 C. Adamo and V. Barone, *J. Chem. Phys.*, 1999, **110**, 6158–6170.

38 R. Krishnan, J. S. Binkley, R. Seeger and J. A. Pople, *J. Chem. Phys.*, 1980, **72**, 650–654.

39 J. Čížek, *Adv. Chem. Phys.*, 1969, **14**, 35.

40 G. D. Purvis and R. J. Bartlett, *J. Chem. Phys.*, 1982, **76**, 1910–1918.

41 K. Raghavachari, G. W. Trucks, J. A. Pople and M. Head-Gordon, *Chem. Phys. Lett.*, 1989, **157**, 479–483.

42 H. J. Werner, P. J. Knowles, G. Knizia, F. R. Manby, M. Schütz, P. Celani, T. Korona, R. Lindh, A. Mitrushenkov and G. Rauhut, *et al.*, *MOLPRO, version 2012.1*.

43 R. Bauernschmitt and R. Ahlrichs, *Chem. Phys. Lett.*, 1996, **256**, 454–464.

44 D. Y. Zubarev and A. I. Boldyrev, *Phys. Chem. Chem. Phys.*, 2008, **10**, 5207–5217.

45 M. J. Frisch, G. W. Trucks, H. B. Schlegel, G. E. Scuseria, M. A. Robb, J. R. Cheeseman, G. Scalmani, V. Barone, B. Mennucci and G. A. Petersson, *et al.*, *Gaussian 09, Revision D.01*, Gaussian, Inc., Wallingford, CT, 2009.

46 C. Gonzalez and H. B. Schlegel, *J. Chem. Phys.*, 1989, **90**, 2154–2161.